

# UC Merced

## UC Merced Previously Published Works

### Title

The effect of Fe-anion interactions on corrosion of ferrous surfaces by phosphonium ionic liquids

### Permalink

<https://escholarship.org/uc/item/3pg689v0>

### Authors

Liu, Ting  
Rahman, Hafizur  
Menezes, Pradeep L  
[et al.](#)

### Publication Date

2023-11-01

### DOI

10.1016/j.corsci.2023.111734

### Supplemental Material

<https://escholarship.org/uc/item/3pg689v0#supplemental>

### Copyright Information

This work is made available under the terms of a Creative Commons Attribution-NonCommercial-NoDerivatives License, available at <https://creativecommons.org/licenses/by-nc-nd/4.0/>

Peer reviewed

# The effect of Fe-anion interactions on corrosion of ferrous surfaces by phosphonium ionic liquids

Ting Liu,<sup>†,¶</sup> Md Hafizur Rahman,<sup>‡,¶</sup> Pradeep L. Menezes,<sup>‡</sup> and Ashlie Martini<sup>\*,†</sup>

<sup>†</sup>*Department of Mechanical Engineering, University of California Merced, 5200 Lake Rd,  
1 Merced, 95343, CA, USA*

<sup>‡</sup>*Department of Mechanical Engineering, University of Nevada Reno, 1664 N Virginia St,  
89557, Reno, NV, USA*

<sup>¶</sup>*Joint first-author, the two authors contributed equally to this paper.*

E-mail: [amartini@ucmerced.edu](mailto:amartini@ucmerced.edu)

Phone: +1 (209) 228-2354

## Abstract

2  
3 Experiments and simulations were used to investigate interactions between ferrous  
4 surfaces and trihexyltetradecylphosphonium benzoate or salicylate. Differences be-  
5 tween the ionic liquids were observed in open circuit potential, potentiodynamic polar-  
6 ization, cyclic potentiodynamic polarization, electrochemical impedance spectroscopy,  
7 and long-duration corrosion tests. While both ionic liquids were far less corrosive than  
8 water, salicylate exhibited slower charge transfer and lower surface protection poten-  
9 tial than benzoate. These observations were analyzed using simulations of chemical  
10 reactions between ions and an ideal Fe(100) surface. Simulation results showed that  
11 salicylate and benzoate differed in their bonding configurations and orientations, sug-  
12 gesting distinct adsorption mechanisms for these similar ionic liquids.

## 13 Introduction

14 Room temperature ILs are a class of organic salts that are liquid at ambient temperature.<sup>1,2</sup>  
15 ILs have many advantages compared to conventional organic compounds in terms of chemical,  
16 physical, thermal, and biological properties.<sup>2,3</sup> For example, ILs have high thermal and  
17 chemical stability<sup>3-5</sup> and low vapor pressure.<sup>6</sup> Some ILs are also miscible in both water and  
18 oil.<sup>7-9</sup> There are anions, such as salicylate, benzoate, and saccharinate, that can be extracted  
19 from plants<sup>10</sup> and numerous studies have investigated ILs that can be recycled and reused  
20 without volume loss.<sup>11-15</sup> Therefore, ILs are considered to be promising green engineering  
21 liquids that offer a potential solution to challenges associated with both solvent emission and  
22 catalytic recycling.<sup>16,17</sup> These advantages make ILs useful for a diverse range of applications  
23 such as lubricants, battery electrolytes, heat transfer fluids, solvents for coating materials,  
24 additives in polymeric materials, and more.<sup>2-4,10,18-23</sup>

25 In many applications, ILs are in direct contact with a metal surface and form a solid-  
26 liquid interface. In such cases, ILs have been found to form adsorption layers composed of  
27 cations, anions, and their decomposition products. The adsorption layers can have either  
28 a corrosive or protective effect, depending on the combination of IL and metal, as well as  
29 on temperature.<sup>24</sup> ILs are usually less corrosive than typical oxidizing species like neutral  
30 sodium chloride solution, acidic or alkaline solution, and oxygen,<sup>25-33</sup> so they can be used  
31 as corrosion inhibitors for metal surfaces like carbon steel, stainless steel, magnesium, cop-  
32 per, and zinc.<sup>20,34-37</sup> However, many ILs are highly polar and have low vapor pressures, and  
33 therefore can be more corrosive to metal surfaces than traditional organic solvents.<sup>2,38</sup> Gen-  
34 erally, corrosion is a concern because it can reduce the strength and durability of equipment  
35 and structures.<sup>38,39</sup> To minimize corrosion in applications involving ILs, it is important to  
36 understand the mechanisms by which ILs interact with and affect corrosion of metal surfaces.

37 There have been a number of experimental studies that have examined the corrosion of  
38 metals in contact with ILs. The rate of corrosion of metals interacting with ILs has been  
39 measured by the weight loss method using a rotating cage experiment.<sup>38,40,41</sup> Electrochemical

40 tests, like corrosion potential, corrosion current density, and electrochemical impedance spec-  
41 troscopy, have also been applied to measure corrosivity of ILs.<sup>25,40-44</sup> Such studies reported  
42 that corrosion processes were controlled by charge transfer at the metal/IL interface<sup>25,41,42,45</sup>  
43 and the corrosivity of ILs strongly depends on the surface material and morphology, the  
44 presence of impurities, and the temperature.<sup>25,38-43,46,47</sup> Corrosion of metals by ILs has also  
45 been shown to be affected by the chemical nature of the IL cation and anion.<sup>24,25,38,39,43,44,47,48</sup>

46 The cation can affect the way that ILs interact with metal surfaces and, therefore, the cor-  
47 rosion of the metal.<sup>24,44,47,48</sup> For example, (2-hydroxyethyl)-trimethyl-ammonium bistriflim-  
48 ide (choline NTF2) caused less corrosion of a copper surface than butyl-trimethyl-ammonium  
49 NTF2.<sup>24</sup> The incorporation of a hydroxyl group into the cation alkyl side chain was found  
50 to decrease corrosivity.<sup>42</sup> Electrochemical tests showed that protic ILs had a narrower elec-  
51 trochemical stability window and were generally more reactive toward metals than aprotic  
52 ILs.<sup>44</sup> Corrosion of aluminium and copper in imidazolium-based ILs with different alkyl  
53 chain lengths showed that corrosion decreased with increasing alkyl chain length.<sup>47</sup> For steel  
54 surfaces, alkyl substituents like polar groups, fragments, conjugated bonds, and various het-  
55 eroatoms in the cation structure led to lower corrosion rate due to the improved adsorption  
56 of cations on the surface.<sup>48</sup>

57 It has also been reported that the anion moiety plays the dominant role in corrosion of  
58 metal surfaces<sup>43,44,49,50</sup> since the polarization behavior of ILs is mainly governed by anions.<sup>43</sup>  
59 For example, anions like tosylate and dimethyl phosphate generally had higher corrosivity on  
60 carbon steel and aluminium than ethyl sulfate, octyl sulfate, and chloride.<sup>38</sup> Severe corrosion  
61 on iron based alloys was found for choline methanesulfonate while choline NTF2 exhibited  
62 significantly lower corrosiveness.<sup>42</sup> On copper surfaces, 1-ethyl-3-methylimidazolium phos-  
63 phonate ([EMIM][EtPO<sub>3</sub>H]) showed more corrosion than 1-ethyl-3-methylimidazolium octyl-  
64 sulfate ([EMIM][C<sub>8</sub>H<sub>17</sub>SO<sub>4</sub>]) due to the formation of a soluble phosphonate-copper complex.  
65 Also, 1-hexyl-3-methylimidazolium tetrafluoroborate ([HMIM][BF<sub>4</sub>]) showed more corrosion  
66 than 1-hexyl-3-methylimidazolium hexafluorophosphate ([HMIM][PF<sub>6</sub>]) since the [BF<sub>4</sub>] an-



67 ion formed a soluble species with copper while the  $[\text{PF}_6]$  anion formed a uniform protec-  
68 tive layer on the copper surface.<sup>49</sup> ILs composed of strongly coordinating anions such as  
69 bis(trifluoromethylsulfonyl)imide (TFSI) are more corrosive to metal surfaces than chloroa-  
70 luminate ILs or ILs with weakly coordinating anions such as tetrafluoroborate ( $\text{BF}_4$ ) and  
71 hexafluorophosphate ( $\text{PF}_6$ ) because TFSI can facilitate metal dissolution by forming a tight  
72 solvation layer with dissolved metal ions.<sup>39</sup>

73 Results reported so far have shown that the chemical nature of the ions can affect the  
74 corrosion of metal surfaces interacting with ILs and that the anion plays a key role. However,  
75 the mechanisms by which anions affect metal corrosion are still not fully understood. Here,  
76 we focused on phosphonium-based ILs that are used in various applications where they  
77 come into contact with ferrous materials.<sup>10,22,51,52</sup> We specifically studied trihexyltetradecyl-  
78 cyolphosphonium benzoate ( $[\text{P6,6,6,14}][\text{Benz}]$ ) and trihexyltetradecylphosphonium salicylate  
79 ( $[\text{P6,6,6,14}][\text{Sali}]$ ). These ILs have been used as lubricants for stainless steel<sup>53</sup> and the an-  
80 ions are derived from natural organic sources.<sup>10</sup>  $[\text{P6,6,6,14}][\text{Benz}]$  and  $[\text{P6,6,6,14}][\text{Sali}]$  were  
81 also chosen because they have the same cation but slightly different anions, which enabled  
82 isolation of the effect of the anion. First, we characterized corrosion of steel in the pres-  
83 ence of phosphonium ILs experimentally. Then, we used reactive molecular dynamics (MD)  
84 simulations to investigate ion-surface interactions and reactions to identify and understand  
85 differences between the two anions.

## 86 **Methods**

### 87 **Corrosion Experiments**

88 The two ionic liquids,  $[\text{P6,6,6,14}][\text{Benz}]$  and  $[\text{P6,6,6,14}][\text{Sali}]$  were synthesized using trihexyl-  
89 tetradecylphosphonium chloride and sodium benzoate, or sodium salicylate through ion ex-  
90 change reaction of trihexyl tetradecyl phosphonium chloride and sodium benzoate/salicylate,  
91 as reported in previous literature.<sup>10,14,54</sup> The produced ionic liquids were dried at 80°C, under

92 vacuum for at least 6 hours and Fourier Transform Infrared Spectroscopy (FTIR) analysis  
 93 was done to confirm the absence of any water peak. The dried ionic liquids were kept at  
 94 room temperature (RT) inside a humidity-controlled desiccator ( $10 \pm 5$  %RH) before use.  
 95 Atomic representations of the individual ions are shown in Fig. 1.

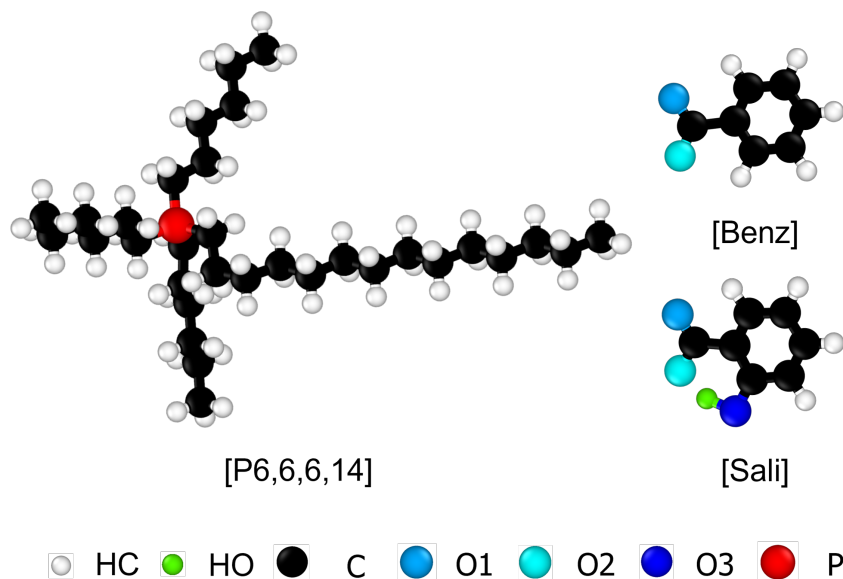


Figure 1: Chemical structures of the [P6,6,6,14] cation, [Benz] anion, and [Sali] anion evaluated in current study. HC: hydrogen atoms bonded to carbon atoms; HO: hydrogen atoms bonded to oxygen atoms; O1: oxygen type 1 of the carboxyl group; O2: oxygen type 2 of the carboxyl group; O3: oxygen atom in the hydroxyl group.

96 The chemical structures of the ILs were characterized using FTIR and  $^1\text{H}$  Nuclear Mag-  
 97 netic Resonance (NMR) spectroscopy. FTIR analyses were performed using a Nicolet FTIR  
 98 (Model:  $iS^{TM}$  380, Thermo Scientific).  $^1\text{H}$  NMR analysis of the neat ILs was carried out  
 99 using an Agilent 500-MHz NMR spectroscope. Deuterated chloroform ( $\text{CDCl}_3$  having D,  
 100  $99.8\%+0.05\%$  V/V TMS) was used as the solvent to carry out the experiments. The results  
 101 were analyzed using MestReNova software.

102 FTIR spectra for the two phosphonium ILs are shown in Fig. S1. For both ILs, prominent  
 103 peaks were observed for alkyl  $sp^3$  C-H bonds ( $2750\text{-}3000\text{ cm}^{-1}$ ) corresponding to the long  
 104 alkyl chain in the cation, and aromatic C=C bonds ( $1450\text{-}1600\text{ cm}^{-1}$ ) that are present in  
 105 the aromatic ring in the anion moieties. Similar spectra for these two ILs were reported

106 previously.<sup>54</sup>

107 Structural confirmation was further obtained from <sup>1</sup>H NMR analyses. Fig. S2(a) shows  
108 the <sup>1</sup>H NMR spectrum for the [P6,6,6,14][Sali]. Here, eight multiplets (A-H) are observed,  
109 among which four (A, B, C and D) are in the aromatic region (6-8 ppm).<sup>55</sup> The integral value  
110 for these four multiplets was four, corresponding to the number of proton nuclei present in the  
111 aromatic ring structure of salicylate anion. Among the other four multiplets, F is located in  
112 the methyl group region (-1 to 4) and corresponds to the four methyl groups (-CH<sub>3</sub>) present  
113 at the four ends of the cation side chains.<sup>55</sup> E, G, and H multiplets are located within  
114 the alkyl chain region (1.1-5.2), confirming the 56 proton nuclei present in the four alkyl  
115 chain branches of the cation.<sup>55</sup> This is consistent with results for [P6,6,6,14][Sali] previously  
116 reported.<sup>54</sup> Similarly, in Fig. S2(b), the <sup>1</sup>H spectrum for [P6,6,6,14][Benz] is presented,  
117 where 73 proton nuclei are confirmed within the ionic liquid structure, again consistent with  
118 literature.<sup>54</sup>

119 To study the corrosion behavior of steel, AISI 52100 steel surfaces were prepared with  
120 an average surface roughness (Sa) of 0.16 μm. Open circuit potential (OCP) measurements,  
121 potentiodynamic polarization (PDP), and cyclic potentiodynamic polarization (CPDP) scans  
122 of the steel specimens were carried out for the neat ILs and for water (as a reference). A three-  
123 electrode electrochemical cell connected to a Gamry Reference 1010 potentiostat (Gamry  
124 Instruments, Warminster, PA, USA) was used to carry out the OCP, PDP, and CPDP  
125 investigations. A standard saturated calomel electrode (SCE) was used as the reference  
126 electrode, and a graphite rod was used as the counter electrode. The AISI 52100 steel  
127 specimen was used as the working electrode in the three-electrode setup. A 0.315 cm<sup>2</sup> surface  
128 area of the working electrode was exposed to each liquid ([P6,6,6,14][Benz], [P6,6,6,14][Sali],  
129 and water) separately over 60 mins in each OCP test. After this duration, the electrochemical  
130 system reached a steady-state potential. At this condition, the PDP tests were carried out  
131 for each test liquid at a scan rate of 1 mV/s from an initial voltage of -0.5 V to a final voltage  
132 of 1.5 V, with respect to OCP. Similarly, the CPDP tests were carried out at the steady state

133 potential with a 1 mV/s scan rate for [P6,6,6,14][Sali] and [P6,6,6,14][Benz]. Each test was  
134 repeated at least twice.

135 The surface topographies were recorded after the electrochemical tests using a profilome-  
136 ter (Rtec Instruments, CA, USA). Then, to characterize the long-term corrosion behavior of  
137 the ILs, AISI 52100 steel samples were submerged in [P6,6,6,14][Benz] or [P6,6,6,14][Sali] for  
138 28 days, and their surface topographies were recorded using the profilometer. To investigate  
139 the corrosion mechanisms, Electrochemical Impedance Spectroscopy experiment was carried  
140 out using a two-electrode system using the Gamry 1010 potentiostat from an initial frequency  
141 of  $10^9$  Hz to a final frequency of 0.01 Hz. FTIR scans were also carried out to detect any  
142 variation in the IL samples before and after long term corrosion tests. Finally, the corroded  
143 surfaces were analyzed using a Renishaw InVia Raman equipment between  $200\text{-}1400\text{ cm}^{-1}$   
144 wavenumbers.

## 145 Reactive Molecular Dynamics Simulation

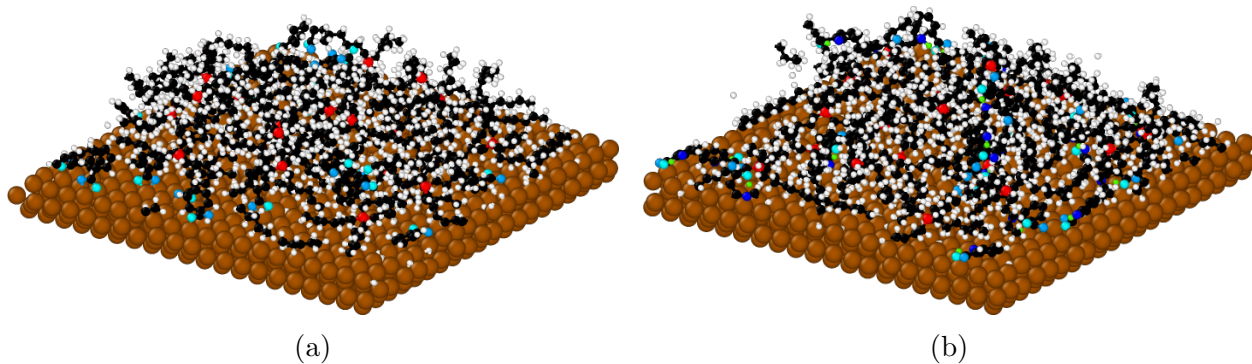


Figure 2: Perspective-view snapshots at the end of the simulations at 300 K for (a) [P6,6,6,14][Benz] and (b) [P6,6,6,14][Sali].

146 Reactive MD simulations of [P6,6,6,14][Benz] and [P6,6,6,14][Sali] on an ideal  $56.8 \times$   
147  $56.8 \text{ \AA}$  Fe(100) surface were performed to investigate the surface interactions and reactions  
148 of these ions. The model system comprised a body-centered cubic Fe(100) slab and 20 ion  
149 pairs in a periodic simulation box. Since the two ILs were characterized experimentally at  
150 100% concentration in experiments, the effect of solvent molecules or other impurities on

151 the adsorption process was not modeled. The structures of the individual ions are shown in  
152 Fig. 1. The ion models were created by Packmol<sup>56</sup> and 20 ion pairs of either [P6,6,6,14][Benz]  
153 or [P6,6,6,14][Sali] were randomly placed 1 nm above the Fe(100) surface. For the crystal  
154 structure of ferrous surface, the most commonly used iron surfaces used to mimic ferrous  
155 metals in MD simulations are (110), (100) and (001).<sup>57</sup> All these are simple approximations  
156 of steel and here we chose Fe(100) as representative.

157 All simulations were performed using the open-source Large-scale Atomic/Molecular Mas-  
158 sively Parallel Simulator (LAMMPS) package.<sup>58</sup> Simulations were based on the ReaxFF force  
159 field. ReaxFF parameters for P/C/H/O were taken from Ref.<sup>59</sup> and parameters for interac-  
160 tions with Fe were taken from Ref.<sup>60</sup> These force field parameters have undergone extensive  
161 validation and benchmarking against experimental data and density functional theory (DFT)  
162 calculations. Particularly, parameters for P/C/H/O interactions were reported to give good  
163 agreement with DFT energies for C–O bond dissociation, P–C bond dissociation, and C–P–C  
164 angle distortion. Additionally, the density of phosphonium glycinate and its mixture with  
165 CO<sub>2</sub> calculated using the ReaxFF force field matched well with experimental values.<sup>59</sup> Most  
166 relevant to the current study, this parameter set was used previously to model thermal de-  
167 composition of phosphonium benzoate and phosphonium salicylate with results that agreed  
168 well with experimental observations.<sup>5</sup> Parameters for interactions between Fe and P/C/H/O  
169 were validated by reproducing energies calculated using DFT for Fe–O–P and Fe–P–O an-  
170 gles, Fe–P bond dissociation, Fe–O–P angle bending, and binding energies for P and PO on  
171 an Fe(100) surface.<sup>60</sup> This parameter set was used previously to model thermal decomposi-  
172 tion of tricresyl phosphate on ferrous surfaces where simulation-calculated reaction products  
173 were consistent with those measured in experiments.<sup>61</sup>

174 After energy minimization, the simulations were performed with a canonical ensemble  
175 with a time step of 0.25 fs. The temperature was maintained at 300 K with a damping  
176 parameter of 25 fs using a Nosé–Hoover thermostat.<sup>62</sup> During this simulation, the ions ap-  
177 proached and reacted with the surface atoms. It was found that the number of ion-surface

178 bonds reached steady-state after about 0.6 ns at 300 K. Therefore, the simulations were  
179 performed for a total duration of 1 ns by which time the potential energy of the simulation  
180 system and number of bonds had reached steady state. Simulations were also run at 400 K  
181 and 500 K for 1 ns. Figs. 2 show snapshots from the end of representative simulations after  
182 reactions between the ions and surface reached steady state. Chemical bonding between  
183 atoms in ILs and Fe atoms in surface was analyzed based on the ReaxFF bond table using  
184 user-defined Python scripts. Results were averaged over 20 time frames during the last 25  
185 ps of the simulation.

## 186 Results and Discussion

187 The OCP results for the AISI 52100 steel with the two phosphonium ILs as well as with  
188 water for reference are shown in Fig. 3. It has been reported the OCP is a measure of the  
189 corrosion potential of electrolytes.<sup>63</sup> Both ILs had much lower corrosion potential than the  
190 water. Comparing the two ILs, the stable voltage recorded for [P6,6,6,14][Sali] was -0.12 V  
191 and, for [P6,6,6,14][Benz], it was -0.24 V, indicating [Sali] has lower corrosion potential than  
192 [Benz]. Profilometer images taken after the electrochemical tests are also shown in Fig. 3.  
193 Significant pitting occurred for water whereas, for both ILs, the pitting marks were shallow  
194 and small.

195 The PDP curves of the steel surfaces for the two ILs and water are reported in Fig. 4.  
196 These results provide an estimation of relative current flow above OCP and can be used to  
197 assess the relative corrosiveness of different electrolytes for a given metal.<sup>64</sup> The corrosion  
198 current density was obtained from the polarization curve using the Tafel extrapolation tech-  
199 nique.<sup>65</sup> The measured current densities for [P6,6,6,14][Sali], [P6,6,6,14][Benz], and water  
200 were 0.12  $\mu\text{A}/\text{cm}^2$ , 0.30  $\mu\text{A}/\text{cm}^2$ , and 5.8  $\mu\text{A}/\text{cm}^2$ , respectively. This shows that the water  
201 was much more corrosive than the ILs.

202 The corrosion rate (mpy) was calculated using the Tafel extrapolation method as  $CR =$

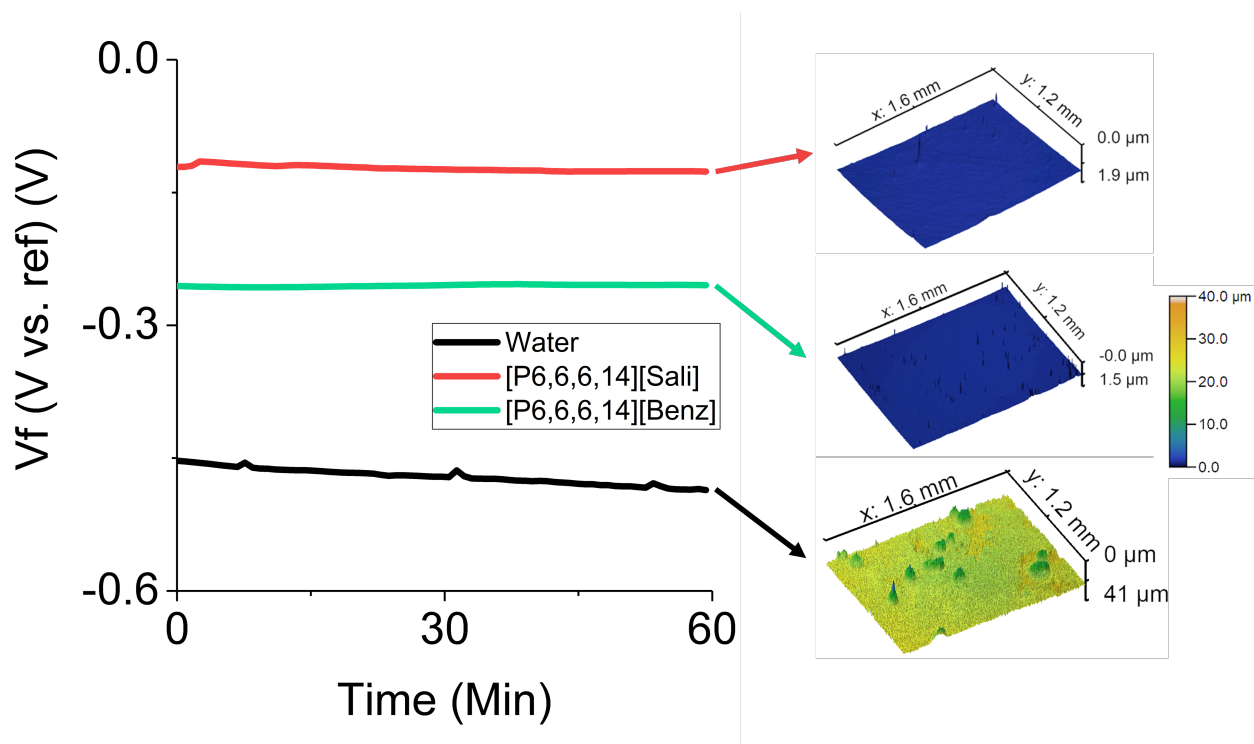


Figure 3: Representative open circuit potential of two ILs and water. To the right are shown representative profilometer images of the steel surfaces taken after the test. The color scale is inverted in the topography images such that large positive values correspond to deep pits. Each test was repeated twice.

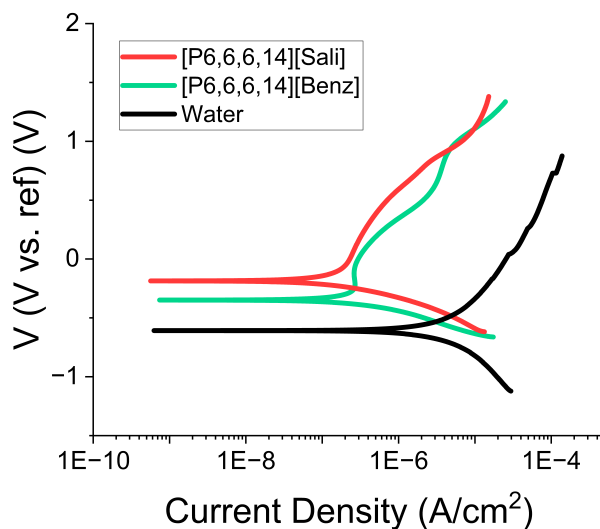


Figure 4: Representative potentiodynamic polarization curves for the two ILs and water. Each test was repeated twice.

203  $(0.13 \times I_{corr} \times E.W.)/d$ , where  $I_{corr}$  is the corrosion current density in  $A/cm^2$ ,  $E.W.$  is  
 204 the equivalent weight of the corroding species, which is 25.59 for AISI 52100 steel, and  $d$  is  
 205 the density of corroding species, which is  $7.81 \text{ g/cm}^3$  for AISI 52100 steel. The corrosion  
 206 rates obtained for [P6,6,6,14][Sali], [P6,6,6,14][Benz], and water were  $0.052 \pm 0.005$ ,  $0.112 \pm$   
 207  $0.028$ , and  $3.56 \pm 1.216$  mpy, respectively. This confirms that the corrosion of steel by the  
 208 ionic liquids was significantly lower than by water.

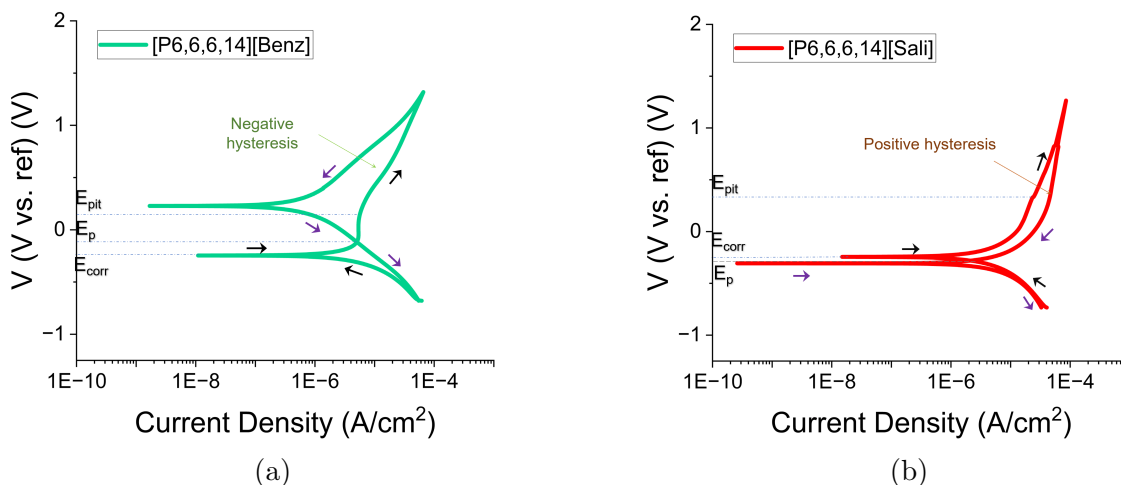


Figure 5: Representative cyclic potentiodynamic polarization curves for (a) [P6,6,6,14][Benz] and (b) [P6,6,6,14][Sali] with black arrows indicating forward scan and purple arrows for the reverse scan. Each test was repeated twice.

Table 1: Cyclic potentiodynamic polarization analysis.

ILs	$E_{pit}$ (V)	$E_{corr}$ (V)	$E_p$ (V)	Hysteresis type
[P6,6,6,14][Benz]	0.21	-0.25	-0.15	Negative
[P6,6,6,14][Sali]	0.75	-0.20	-0.30	Positive

209 The CPDP results for the two ILs are shown in Fig. 5, where horizontal lines identify the  
 210 key parameters: pitting potential ( $E_{pit}$ ), corrosion potential ( $E_{corr}$ ), and protection potential  
 211 ( $E_p$ ). As shown in Fig. 5 and Table 1,  $E_{pit}$  is lower for [P6,6,6,14][Benz] than [P6,6,6,14][Sali],  
 212 indicating the steel is more susceptible to the initiation of corrosion pits in the presence of  
 213 the [Benz]-containing IL. However, for [P6,6,6,14][Benz],  $E_p$  is above  $E_{corr}$  with a negative  
 214 hysteresis loop, indicating that the passive film damage repaired itself during the cathodic



215 polarization phase such that further pitting was not initiated.<sup>66</sup> Negative hysteresis typically  
 216 occurs in CPDP when, for the reverse voltage sweep, the current density goes lower than the  
 217 forward cycle<sup>67</sup> (indicated by the purple arrows in Fig. 5(a)). As a result, the  $E_p$  stays above  
 218 the  $E_{corr}$ . In contrast, positive hysteresis occurs when the current density in the reverse cycle  
 219 becomes more than the first cycle, depicting  $E_p < E_{corr}$ .<sup>67</sup> As observed in Fig. 5(b),  $E_p$  is  
 220 below  $E_{corr}$  for [P6,6,6,14][Sali] with a positive hysteresis loop, indicating a lack of effective  
 221 protection or insufficient formation of a protective film to prevent pitting propagation.

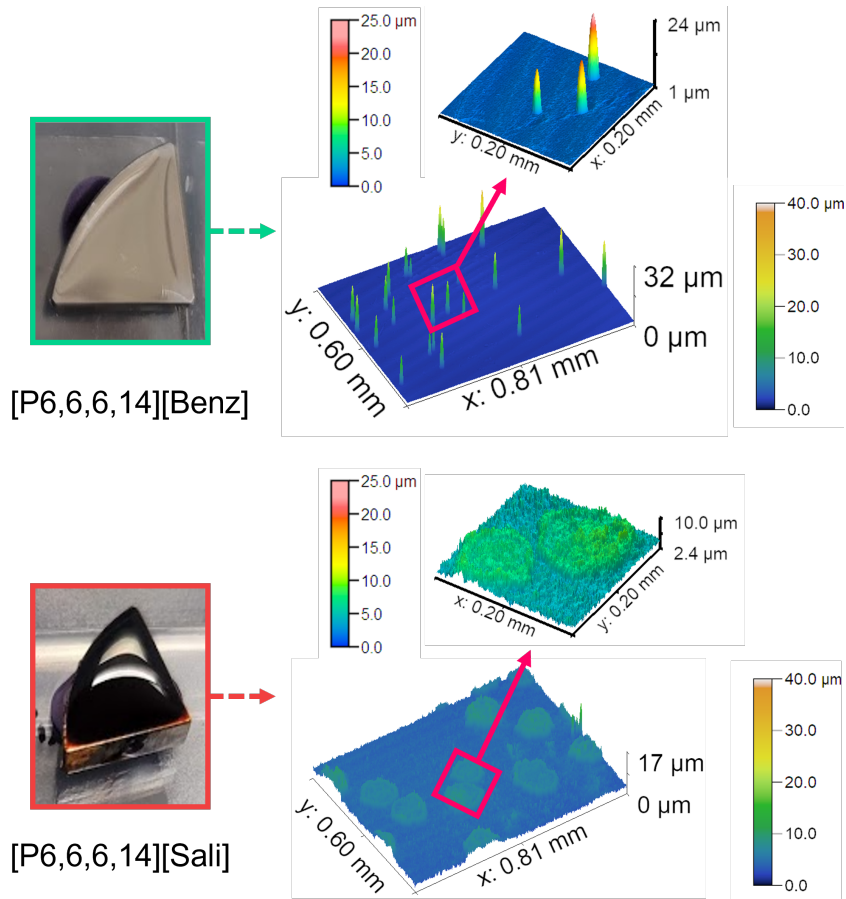


Figure 6: Photos and inverted topography images of steel from the experimental corrosion test of [P6,6,6,14][Benz] and [P6,6,6,14][Sali] on AISI 52100 steel at room temperature after four weeks. The color scale is inverted in the topography images such that large positive values correspond to deep pits.

222 The results from the CPDP tests indicated the two ILs should have different pitting  
 223 behavior on steel. Next, a long duration corrosion study was carried out to directly observe

224 pitting. Photos and surface topography images of the steel surfaces after the experimental  
 225 corrosion tests with [P6,6,6,14][Benz] and [P6,6,6,14][Sali] after four weeks are shown in  
 226 Fig. 6. With both ILs, pits formed on the surfaces due to corrosion and it was observed that  
 227 both surfaces got rougher. The average surface roughness, 0.16  $\mu\text{m}$  before testing, increased  
 228 to 0.92  $\mu\text{m}$  for [P6,6,6,14][Sali] and 0.22  $\mu\text{m}$  for [P6,6,6,14][Benz]. There are also distinct  
 229 differences in the surface morphologies, with narrow deep pits observed for [P6,6,6,14][Benz]  
 230 and broad shallow pits for [P6,6,6,14][Sali]. In the case of [P6,6,6,14][Benz], the average  
 231 maximum roughness valley depth (Rvm) was  $18.94 \pm 4.41 \mu\text{m}$  but only about 0.2% of the  
 232 surface area was pitted. In the case of [P6,6,6,14][Sali], the average depth of the pits was  
 233 much less, with an Rvm of  $2.23 \pm 0.58 \mu\text{m}$ , but the pit area was much larger, covering 11.9%  
 234 of the surface. The deep purple color for the case of [P6,6,6,14][Sali] indicates the formation  
 235 of iron-salicylate.<sup>68</sup>

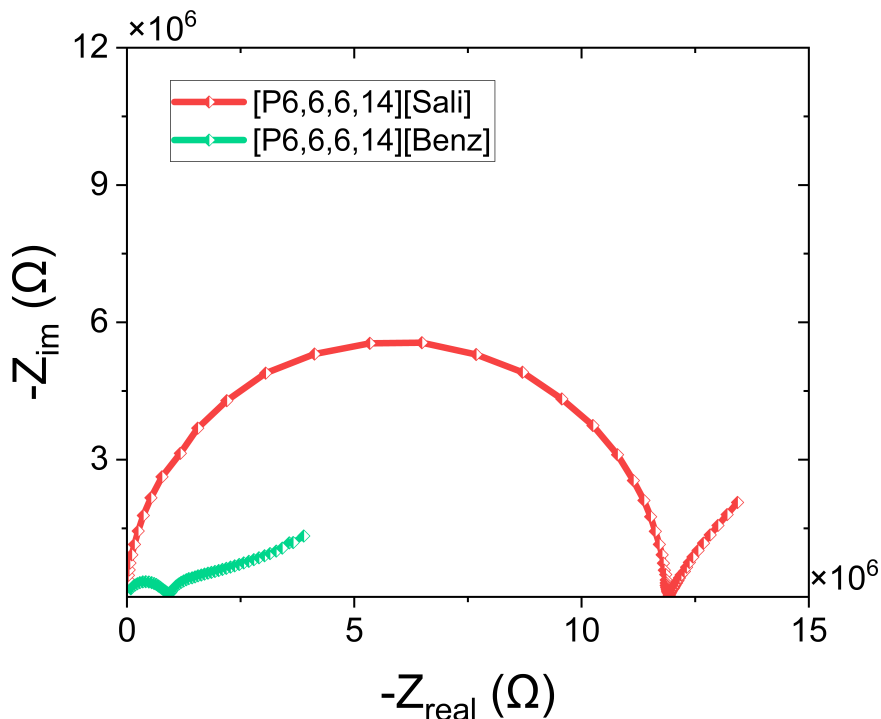


Figure 7: Representative Nyquist plot from the electrochemical impedance spectroscopy of two ILs. Each test was repeated three times.

236 Fig. 7 shows the Nyquist plots for the studied ILs. For both ILs, the curve contains

237 a semi-circle representing the charge transfer process, and an upward line, representing  
 238 the diffusion control process.<sup>69</sup> The wider semi-circle for [P6,6,6,14][Sali] indicates a slower  
 239 charge transfer process than [P6,6,6,14][Benz]. This could be attributed to the smaller and  
 240 symmetric anion shape of benzoate, that vertically orients onto the surface, allowing more  
 241 ions (cation and anion) to come close to the surface<sup>70</sup> and participate in charge transfer. As a  
 242 result, the charge transfer for [P6,6,6,14][Benz] was likely to be higher than [P6,6,6,14][Sali].  
 243 Higher charge transfer increases the molecular adsorption on metal.<sup>71</sup> Possibly for this reason,  
 244 [P6,6,6,14][Benz] was better able to passivate the surface than [P6,6,6,14][Sali]. The linear  
 245 portion in the Nyquist plot indicates a diffusion control reaction, meaning the ions are  
 246 diffused towards the steel surface due to the concentration gradient.<sup>72</sup> Both [P6,6,6,14][Sali]  
 247 and [P4,4,4,14][Benz] exhibited diffusion, which could have facilitated electron or proton  
 248 transfer reactions at the interface.<sup>73</sup>

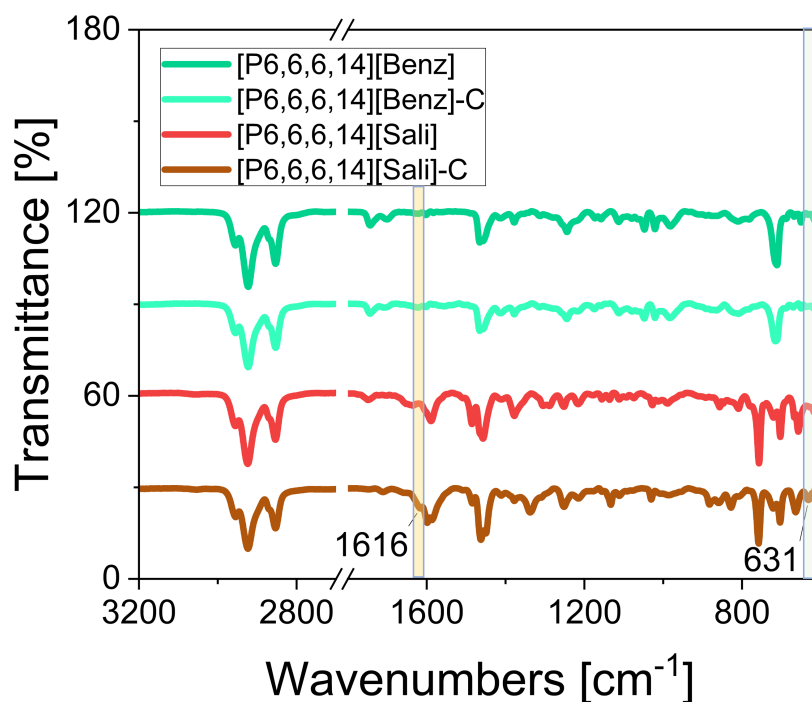


Figure 8: FTIR spectroscopy of the ILs before and after the long-term corrosion test (C indicates the IL sample after corrosion test).

249 To understand any chemical change to the ILs after the long term corrosion test, FTIR

250 analysis was done. Fig. 8 shows the FTIR analysis of the ionic liquids before and af-  
 251 ter the long-term corrosion tests. Fig. 8 shows that no significant change occurred for  
 252 [P6,6,6,14][Benz] after corrosion (indicated with a C in Fig. 8). However, some deviations  
 253 in the FTIR spectra were identified for [P6,6,6,14][Sali]. Particularly, two new peaks were  
 254 observed around  $631\text{ cm}^{-1}$  and  $1616\text{ cm}^{-1}$ , indicating the presence of iron oxide from the  
 255 surface due to the dissolution of iron in the presence of the ionic liquid.

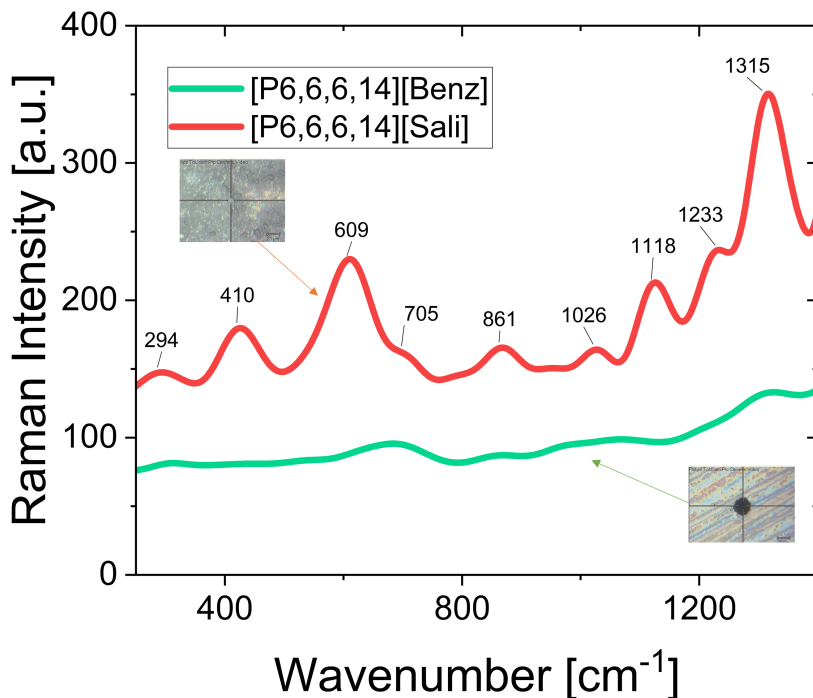


Figure 9: Raman spectroscopy of the corroded surface after the long term corrosion test. The corroded surface profiles observed in the Invia confocal Raman microscope for [P6,6,6,14][Sali] and [P6,6,6,14][Benz] are shown in the inset with the red and green arrows, respectively.

256 To characterize changes to the steel surface after the long-term corrosion test in the  
 257 presence of ILs, Raman spectroscopy was carried out. In Fig. 9, [P6,6,6,14][Sali] exhibits  
 258 prominent peaks at around 294, 410, 609, 705, 1315  $\text{cm}^{-1}$ . These peaks correspond to  $\text{Fe}_2\text{O}_3$   
 259 as reported in the literature.<sup>74</sup> The peak at 861  $\text{cm}^{-1}$  corresponds to C-O-C, which could  
 260 be due to the interaction of oxygen on the anionic moiety with the carbon present in the

261 carbon steel.<sup>75</sup> The peak at  $1026\text{ cm}^{-1}$  could be for the C-H stretch due to the interaction  
 262 of cationic alkyl moiety adsorbed chemically on the surface.<sup>76</sup> Similar peaks were obtained  
 263 with weaker intensity for [P6,6,6,14][Benz] as well. It could be concluded that salicylate,  
 264 having more oxygen in the hydroxyl group, was able to react with surface more and provide  
 265 more oxides than benzoate.

266 The very different types of pitting in the long duration corrosion tests with the two  
 267 ILs can be understood in terms of the results from the OCP, PDP, and CPDP tests. The  
 268 OCP and PDP tests showed that the current density and the corrosion rate were higher  
 269 for [P6,6,6,14][Benz] than [P6,6,6,14][Sali]. Besides, the CPDP results showed that the pit-  
 270 ting potential was lower for [P6,6,6,14][Benz]. However, with [P6,6,6,14][Benz], there was  
 271 sufficient protection by the passive film on steel to limit pitting propagation. Therefore,  
 272 while corrosion was likely to happen more rapidly with [P6,6,6,14][Benz], the protective  
 273 film impeded propagation such that subsequent corrosion occurred near the points of ini-  
 274 tiation, leading to narrow, deep pits. In contrast, while the corrosion rate was slower for  
 275 [P6,6,6,14][Sali], there was an insufficient protective film such that corrosion propagated on  
 276 the surface, resulting in broad, but shallower pits.

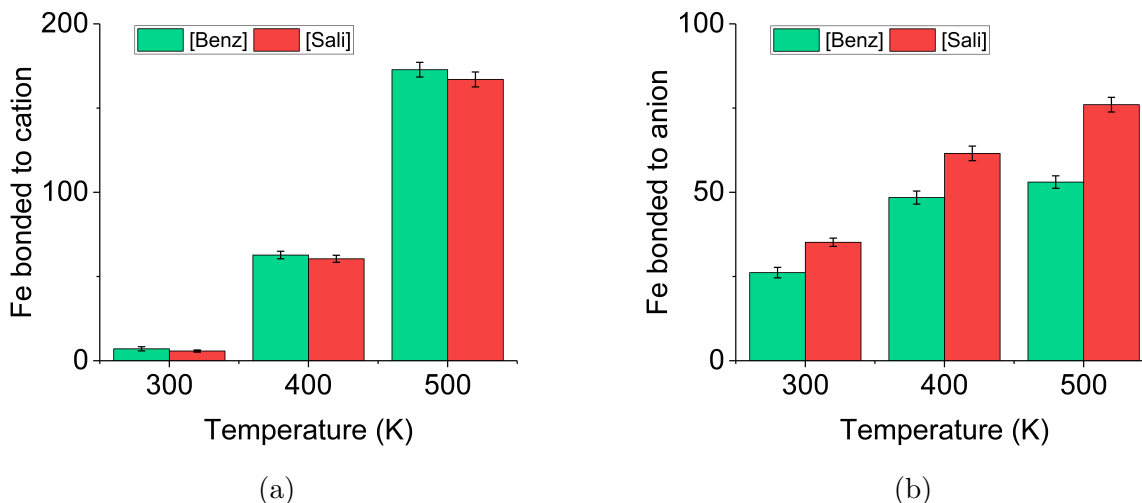


Figure 10: Steady-state number of Fe atoms bonded to (a) cations and (b) anions from simulations of the two ILs interacting with a Fe(100) surface at three different temperatures with error bars showing the standard deviation for three independent tests.

277 To better understand the IL interactions with the steel surface at high temperature,  
278 PDP experiments were carried out at 373 K. Fig. S3(a-b) shows the PDP curves for  
279 [P6,6,6,14][Sali] and [P6,6,6,14][Benz] at room temperature (298 K) and a higher tempera-  
280 ture (373 K). For both ILs, the PDP graph shifted to the right at the higher temperature.  
281 The corrosion current densities at 373 K for [P6,6,6,14][Sali] and [P6,6,6,14][Benz] are 4.9  
282  $A/cm^2$  and 2.3  $A/cm^2$ , respectively. As calculated from two repeated tests, the corrosion rate  
283 associated with [P6,6,6,14][Sali] at 373 K is  $2.37 \pm 0.131$ , which is faster than at room tem-  
284 perature. Similarly, at the higher temperature, a faster corrosion rate of  $0.813 \pm 0.362$  was  
285 observed for [P6,6,6,14][Benz]. At high temperatures, the surface oxidation rate increased  
286 and, therefore, the corrosion rate increased as well.<sup>77</sup>

287 Due to their limited time and size scale, reactive MD simulations cannot explicitly model  
288 material removal through corrosion. However, as a first step, simulations were used to  
289 understand how the ions interact and chemically react with a ferrous surface. First, we  
290 analyzed the bonding between surface Fe atoms and the cations and anions in the ILs. As  
291 shown in Fig. 10, the surface bonding increased with temperature, as expected since more  
292 thermal energy facilitates bond dissociation and formation. There are more cation-Fe bonds  
293 than anion-Fe bonds because there is a greater number of atoms in the cations than the  
294 anions. However, the difference between Fe-cation bonding for the two ILs was negligible in  
295 Fig. 10(a), as expected since the cation is the same. In contrast, the comparison of anion-  
296 surface interactions in Fig. 10(b) shows that the key difference between the ILs is that [Sali]  
297 exhibits more bonding with the surface than [Benz] at any temperature.

298 Therefore, we focused subsequent analysis on interactions between Fe and the anions.  
299 Anion chemisorption reactions can occur through formation of either Fe-C or Fe-O bonds.  
300 The number of Fe atoms bonded to anion C or O atoms is given in Fig. 11. This analysis  
301 shows that bonding with C is dominant for the [Sali] while O bonding is dominant for the  
302 [Benz] at all temperatures. Since the reactions with O atoms are the cause of corrosion,  
303 the Fe-O bonding was further analyzed, where oxygen atoms are identified by the labels in

304 Fig. 2.

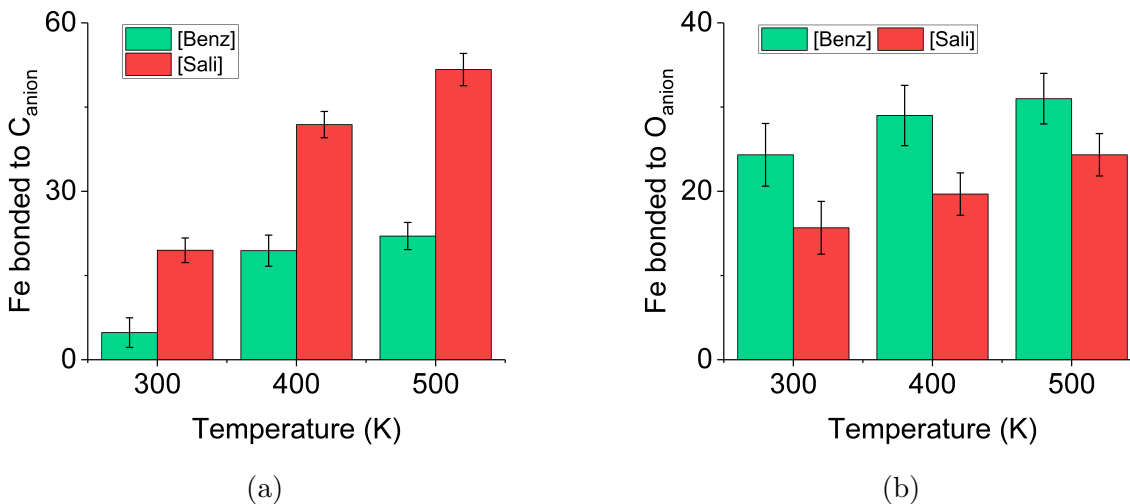


Figure 11: Steady-state number of Fe atoms bonded to (a) C atoms and (b) O atoms in the anions from simulations of the two ILs interacting with a Fe(100) surface at three different temperatures with error bars showing the standard deviation for three independent tests.

305 For [Benz], as shown in Fig. 12(a), the number of Fe–O1 and Fe–O2 bonds was similar  
 306 at all temperatures, as expected since the ion is symmetric. In these simulations, there were  
 307 only two bonding scenarios: (i) Fe–O1 and Fe–O2 (Fe–O1&O2), or (ii) Fe–O1 or Fe–O2 (Fe–  
 308 O1||O2). Snapshots of representative examples of these two bonding scenarios are shown in  
 309 Figs. 12(b) and (c). The likelihood of each bonding scenario was calculated from the number  
 310 of anions exhibiting a given bonding scenario divided by the total number of chemisorbed  
 311 anions. The calculation was performed at the end of the simulation using data from all three  
 312 temperatures (no statistical difference between the temperatures was observed). The anion  
 313 reacted with the surface through Fe–O1&O2 bonding 93.1% of the time, consistent with a  
 314 previous experimental study that reported bonding at the two O atoms in [Benz] and a TiO<sub>2</sub>  
 315 surface.<sup>78</sup> The Fe–O1||O2 bonding scenario was only observed 6.9% of the time.

316 For [Sali], as shown in Fig. 13(a), the reactivity of the O atoms with Fe on the surface  
 317 decreased as O1 > O2 > O3 at all temperatures. The O1 was more reactive than the O2 in  
 318 [Sali] due to the presence of the hydroxyl group. As mentioned in a previous study, the hy-  
 319 droxyl group (H–O3) pointing to O2 indicates intramolecular interaction between the H atom

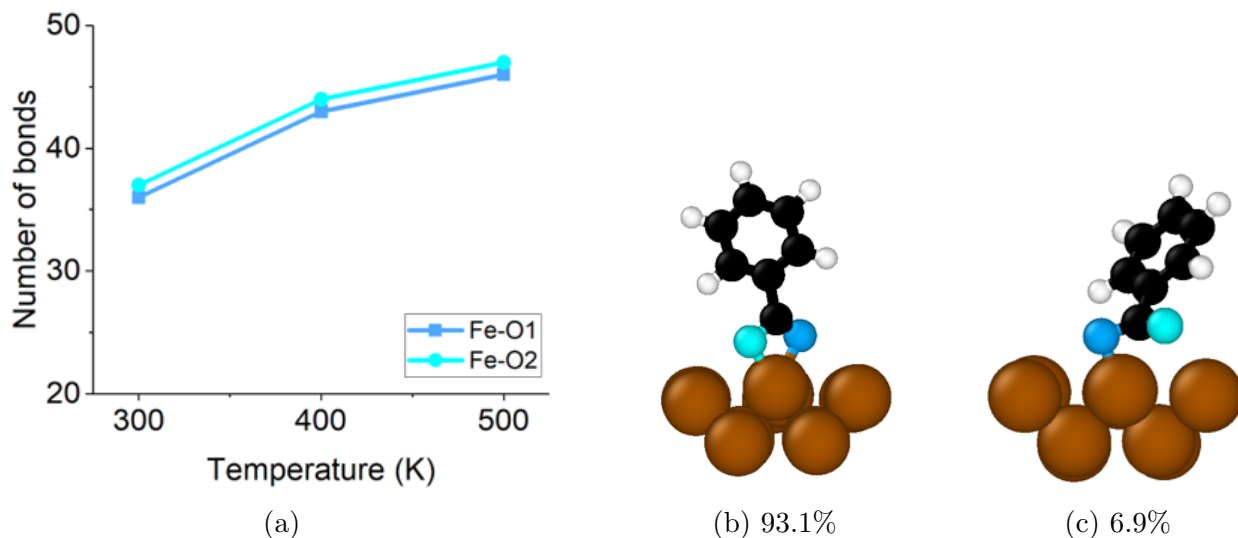


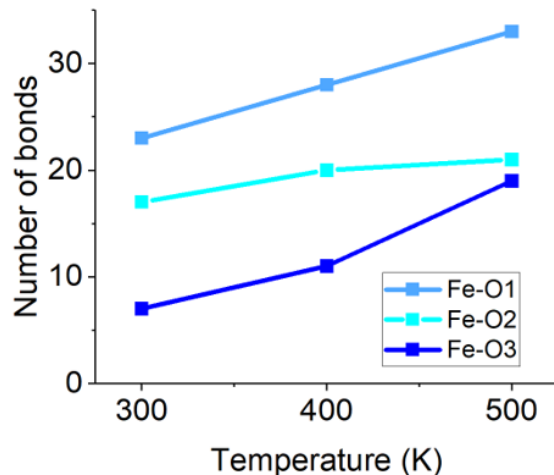
Figure 12: (a) Number of Fe–O1 and Fe–O2 bonds as a function of temperature for [Benz], with representative snapshots of the two possible bonding scenarios (b) Fe–O1&O2 or (c) Fe–O1||O2, and the percent of all bonded anions in which each scenario was observed.

320 in the hydroxyl group and O2, which hinders the ability of O2 to take part in reactions with  
 321 other atoms.<sup>5</sup> For [Sali], there were four bonding scenarios: Fe–O1&O2, Fe–O1&O2&O3,  
 322 Fe–O1, and Fe–O3. This is consistent with the multiple possible bonding scenarios for [Sali]  
 323 on metal surfaces found in previous studies using experiments and simulations showing both  
 324 the hydroxyl group and carboxyl group can interact with metal.<sup>79–83</sup> Like [Benz], for [Sali],  
 325 Fe–O1&O2 bonding was the dominant scenario with a probability of 51.9%. This was fol-  
 326 lowed by Fe–O1&O2&O3 with 22.3%, Fe–O1 with 19.1%, and Fe–O3 with 6.7%. In [Sali],  
 327 both the carboxyl group and the hydroxyl groups can interact with Fe atoms,<sup>84</sup> so there are  
 328 more possible bonding scenarios for [Sali] than [Benz].

329 For both [Benz] and [Sali], the key difference between the different bonding scenarios  
 330 is the orientation of the benzene ring relative to the surface. The orientation of anions has  
 331 previously been found to affect the interaction between ILs and surfaces. For example, anion  
 332 orientation was found to affect metal-IL binding energy,<sup>70,85</sup> IL film formation on alumina,<sup>86</sup>  
 333 and interactions between ILs and graphene.<sup>87</sup> Therefore, the anion orientation for each Fe–O  
 334 bonding scenario was analyzed for both ILs.

335 Anion orientation angle was calculated as the angle between the anion plane (defined





(a)

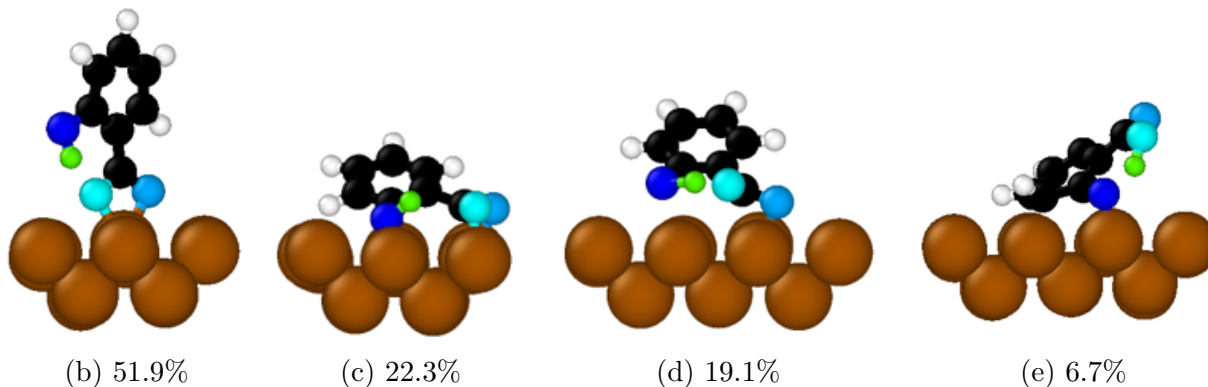


Figure 13: (a) Number of Fe–O1, Fe–O2, and Fe–O3 bonds as a function of temperature for [Sali] with representative snapshots of the four possible bonding scenarios (b) Fe–O1&O2, (c) Fe–O1&O2&O3, (d) Fe–O1 or (e) Fe–O3, and the percent of all bonded anions in which each scenario was observed.

336 by the positions of O1, O2, and the carbon atom in the benzene ring farthest from the  
 337 carboxyl group), and the plane of the Fe(100) surface. This calculation was performed for  
 338 each bonding scenario observed in simulations at all three temperatures (no difference in the  
 339 trends was observed at the different temperatures). As shown in Fig. 14, the anions with  
 340 Fe–O1&O2 bonding tended to be orientated more vertically (angles approaching 90°) than  
 341 the other bonding scenarios for both anions. The frequency of Fe–O1&O2 bonding scenario  
 342 was much higher for [Benz] than [Sali], indicating [Benz] was orientated more vertically relative  
 343 to the ferrous surface than [Sali]. This is consistent with the dominant O bonding for the  
 344 [Benz] and dominant C bonding for the [Sali] observed in Fig. 11.

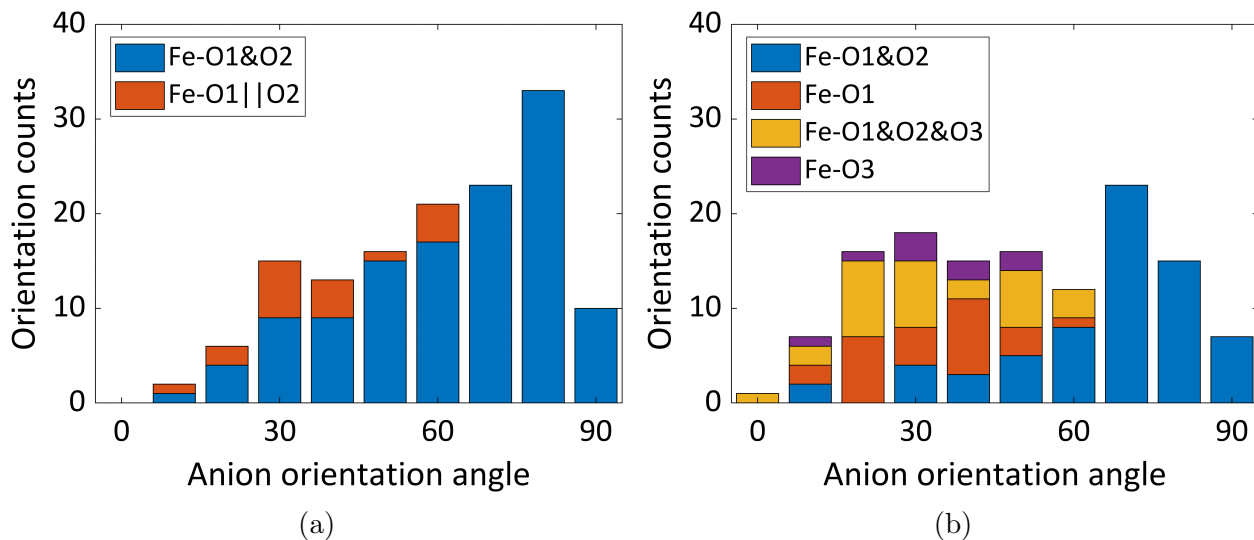


Figure 14: Distribution of the anion orientation angle relative to the surface (at 0°, the benzene ring is parallel to the surface and at 90° the ring is perpendicular to the surface) for the different Fe–O bonding scenarios exhibited by (a) [Benz] and (b) [Sali].

345 As mentioned previously, reactive MD simulations cannot explicitly model corrosion, so  
 346 the simulation results cannot directly explain trends observed in the experiments. However,  
 347 there are some possible implications of the findings from the simulations for corrosion. First,  
 348 the vertical orientation of [Benz] anions enabled more [Benz] anions to reach the surface than  
 349 the [Sali]. This was confirmed by calculating the average anion number density (number of  
 350 ions per nm<sup>2</sup>) chemisorbed on the surface, which was found to be 0.42, 0.58, and 0.62 for  
 351 [Benz] and 0.25, 0.39, and 0.41 for [Sali] at the three different temperatures. A previous  
 352 study also reported that [Benz] can be absorbed more easily on ferrous surfaces compared  
 353 to [Sali].<sup>84</sup> The higher density of [Benz] can lead to a faster rate of charge transfer at the  
 354 metal/IL interface, supporting the observation in the Nyquist plots. This may suggest a  
 355 mechanism to explain the higher OCP voltage magnitude in Fig. 3 and higher PDP current  
 356 flow in Fig. 4 for [P6,6,6,14][Benz] than [P6,6,6,14][Sali].

357 Second, the orientation of the ions on the surface affects the stability of the Fe-anion  
 358 complexes formed. It has been reported previously that Fe-[Sali] complexes are stronger and  
 359 more stable than Fe-[Benz] complexes.<sup>84</sup> Here, the relative stability of the two anions on the  
 360 surface was estimated using the Fe–O bond order available from ReaxFF.<sup>88</sup> The results in

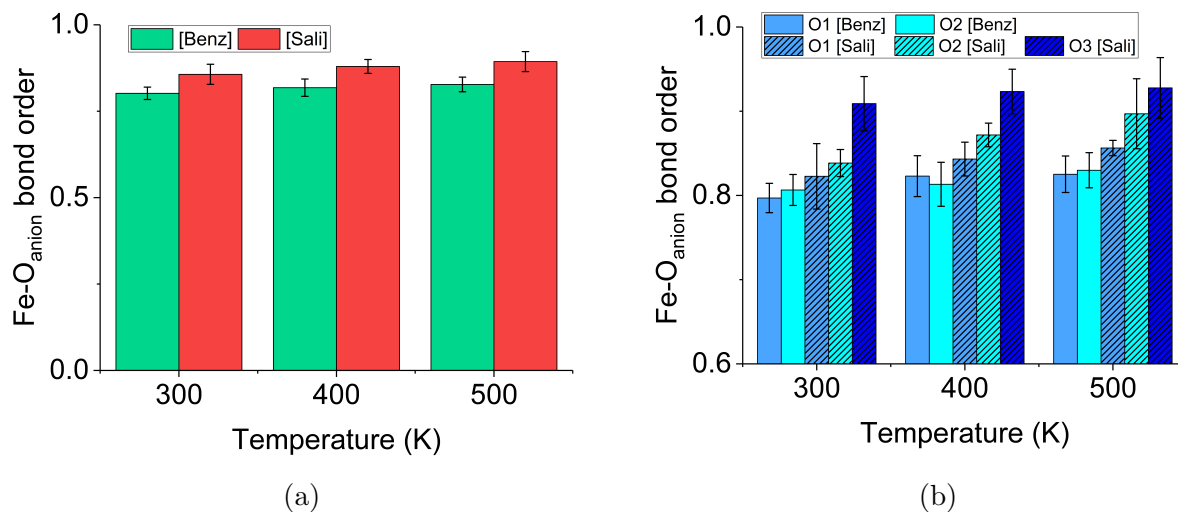


Figure 15: Steady-state Fe–O bond order (a) for the two anions and (b) separated by O type at three different temperatures with error bars showing the standard deviation for three independent tests.

361 Fig. 15(a) show that the bond order was consistently higher for [Sali], indicating stronger  
 362 bonds and greater stability of the Fe–[Sali] complex. The bond order analysis was repeated  
 363 for each oxygen atom separately and, as shown in Fig. 15(b), the strongest Fe–[Sali] bonds  
 364 were for O3. This bonding site was not available in [Benz], leading to lower chemical stability  
 365 of the Fe–[Benz] complex. This can be correlated to the FTIR results in Fig. 8 where the peak  
 366 shape for benzoate did not change whereas, for salicylate, additional peaks for iron oxide  
 367 were detected, which indicates the formation of the iron oxide-salicylate complex. These  
 368 analyses of stability may suggest a mechanism to explain the qualitative differences between  
 369 the ILs in the long-duration corrosion tests in Fig. 6. Since Fe–[benz] complexes are relatively  
 370 unstable chemically, they are more likely to dissociate, promoting dissolution of the surface  
 371 and making available new active sites for subsequent corrosion reactions. The dissolution  
 372 of the ferrous surface is localized around the initial Fe–O bonding leading to, over time,  
 373 the formation of deep and narrow corrosion pits. In contrast, the stability of the Fe–[Sali]  
 374 complexes hinders localized dissolution and leads to subsequent bonding and dissolution over  
 375 a larger area, resulting in the formation of wider and shallower corrosion pits.

## 376 Conclusions

377 Reactive MD simulations of chemical adsorption and experimental corrosion tests were used  
378 to explore the interactions between ferrous surfaces and phosphonium benzoate or phospho-  
379 nium salicylate. From experiments, both ILs showed much less corrosion of steel than water.  
380 However, OCP, PDP, and surface topography analysis showed that the corrosion behavior of  
381 the two ILs differed, where corrosion was likely to be faster and form narrower, deeper cor-  
382 rosion pits for the [Benz]-based IL. Further, EIS and CPDP analyses showed that the charge  
383 transfer at the interface was higher for [Benz], and its protection potential was higher than  
384 [Sali], meaning the surface was passivated and then the passive film protected the surface  
385 from further localized pitting. In contrast, [Sali] experienced slower charge transfer, indicat-  
386 ing that the passive film broke down to initiate more pits, creating a shallower, but wider  
387 pit pattern than [Benz]. While the reactive MD simulations could not directly mimic these  
388 experiments, as a first step towards understand mechanisms, the simulations were used to  
389 investigate IL-surface interactions. The key observations were that the interactions between  
390 Fe and [Benz] were localized at the O atoms in the carboxyl group leading to preferentially  
391 vertical alignment relative to the surface. In contrast, the interactions between Fe and [Sali]  
392 were distributed across the anion such that [Sali] had more possible bonding scenarios and  
393 tended to be oriented parallel to the surface.

394 Both experiments and simulations confirm that the anion plays a critical role in affecting  
395 how ILs react with surfaces, including as part of corrosion processes. The sensitivity of these  
396 interactions to the anion is emphasized by the fact that the chemical difference between  
397 [Benz] and [Sali] is so subtle. For these two anions particularly, the reactive simulations  
398 showed that the orientation of the anion after bonding to the surface can directly affect  
399 chemisorption reactions. This has implications for understanding corrosion mechanisms as  
400 well as other scientific and engineering process that involve ionic liquids in contact with  
401 ferrous surfaces. Lastly, although the current study was focused on the role of anion moiety  
402 and only one Fe surface, the simulation method developed may be used in future work to

403 explore the potential effects of surface inclusions, different metals or surfaces, impurities in  
404 the ILs, or solvents molecules on interactions and reactions between ILs and surfaces.

## 405 **Acknowledgement**

406 The authors acknowledge the support of the National Science Foundation (Grant No. CMMI-  
407 2010205 and 2010584). The authors also appreciate valuable input from Dr. Manish Patel.

## 408 **Supporting Information Available**

409 Supporting Information provides additional analysis from experiments. Contents include  
410 representative FTIR spectroscopy of [P6,6,6,14][Benz] and [P6,6,6,14][Sali], <sup>1</sup>H NMR spectra  
411 for [P6,6,6,14][Benz] and [P6,6,6,14][Sali], and representative potentiodynamic polarization  
412 curves for the two ILs at room temperature and at 373 K.

## 413 **Data Availability**

414 The raw and processed data required to reproduce these findings are available upon request  
415 to the corresponding author.

## 416 **References**

- 417 (1) Lei, Z.; Chen, B.; Koo, Y.-M.; MacFarlane, D. R. Introduction: ionic liquids. *Chem.*  
418 *Rev.* **2017**, *117*, 6633–6635.
- 419 (2) Singh, S. K.; Savoy, A. W. Ionic liquids synthesis and applications: An overview. *J.*  
420 *Mol. Liq.* **2020**, *297*, 112038.
- 421 (3) Joshi, M. D.; Anderson, J. L. Recent advances of ionic liquids in separation science and  
422 mass spectrometry. *RSC Adv.* **2012**, *2*, 5470–5484.

- 423 (4) Greer, A. J.; Jacquemin, J.; Hardacre, C. Industrial applications of ionic liquids.  
424 *Molecules* **2020**, *25*, 5207.
- 425 (5) Khajeh, A.; Rahman, M. H.; Liu, T.; Panwar, P.; Menezes, P. L.; Martini, A. Thermal  
426 decomposition of phosphonium salicylate and phosphonium benzoate ionic liquids. *J.*  
427 *Mol. Liq.* **2022**, *352*, 118700.
- 428 (6) Hallett, J. P.; Welton, T. Room-temperature ionic liquids: solvents for synthesis and  
429 catalysis. 2. *Chem. Rev.* **2011**, *111*, 3508–3576.
- 430 (7) Marsh, K. N.; Boxall, J. A.; Lichtenthaler, R. Room temperature ionic liquids and their  
431 mixtures—a review. *Fluid Phase Equilib.* **2004**, *219*, 93–98.
- 432 (8) Qu, J.; Bansal, D. G.; Yu, B.; Howe, J. Y.; Luo, H.; Dai, S.; Li, H.; Blau, P. J.;  
433 Bunting, B. G.; Mordukhovich, G.; others Antiwear performance and mechanism of an  
434 oil-miscible ionic liquid as a lubricant additive. *ACS Appl. Mater. Interfaces* **2012**, *4*,  
435 997–1002.
- 436 (9) McDaniel, J. G.; Verma, A. On the miscibility and immiscibility of ionic liquids and  
437 water. *J. Phys. Chem. B* **2019**, *123*, 5343–5356.
- 438 (10) Rahman, M. H.; Khajeh, A.; Panwar, P.; Patel, M.; Martini, A.; Menezes, P. L. Recent  
439 progress on phosphonium-based room temperature ionic liquids: Synthesis, properties,  
440 tribological performances and applications. *Tribol. Int.* **2022**, *167*, 107331.
- 441 (11) Abu-Eishah, S. I. Ionic liquids recycling for reuse. *Ionic Liquids-Classes and Properties*  
442 **2011**, 239–272.
- 443 (12) Mai, N. L.; Ahn, K.; Koo, Y.-M. Methods for recovery of ionic liquids—A review.  
444 *Process Biochem.* **2014**, *49*, 872–881.
- 445 (13) Zhou, Y.; Qu, J. Ionic liquids as lubricant additives: a review. *ACS Appl. Mater.*  
446 *Interfaces* **2017**, *9*, 3209–3222.

- 447 (14) Kasar, A. K.; Reeves, C. J.; Menezes, P. L. The effect of particulate additive mixtures  
448 on the tribological performance of phosphonium-based ionic liquid lubricants. *Tribol.*  
449 *Int.* **2022**, *165*, 107300.
- 450 (15) Sivapragasam, M.; Jaganathan, J. R.; Levêque, J.-M.; Moniruzzaman, M.; Mu-  
451 talib, M. A. Microbial biocompatibility of phosphonium-and ammonium-based ionic  
452 liquids. *J. Mol. Liq.* **2019**, *273*, 107–115.
- 453 (16) Hajipour, A.; Rafiee, F. Basic ionic liquids. A short review. *J. Iran. Chem. Soc.* **2009**,  
454 *6*, 647–678.
- 455 (17) Singh, S. K. Solubility of lignin and chitin in ionic liquids and their biomedical appli-  
456 cations. *Int. J. Biol. Macromol.* **2019**, *132*, 265–277.
- 457 (18) Reeves, C. J.; Siddaiah, A.; Menezes, P. L. Ionic liquids: a plausible future of bio-  
458 lubricants. *J. Bio- Tribo-Corros.* **2017**, *3*, 18.
- 459 (19) Welton, T. Ionic liquids: a brief history. *Biophys. Rev.* **2018**, *10*, 691–706.
- 460 (20) Verma, C.; Alrefaee, S. H.; Quraishi, M.; Ebenso, E. E.; Hussain, C. M. Recent devel-  
461 opments in sustainable corrosion inhibition using ionic liquids: A review. *J. Mol. Liq.*  
462 **2021**, *321*, 114484.
- 463 (21) Koutsoukos, S.; Philippi, F.; Malaret, F.; Welton, T. A review on machine learning  
464 algorithms for the ionic liquid chemical space. *Chem. Sci.* **2021**, *12*, 6820–6843.
- 465 (22) Liu, T.; Panwar, P.; Khajeh, A.; Rahman, M. H.; Menezes, P. L.; Martini, A. Review  
466 of Molecular Dynamics Simulations of Phosphonium Ionic Liquid Lubricants. *Tribol.*  
467 *Lett.* **2022**, *70*, 1–24.
- 468 (23) Rahman, M. H.; Liu, T.; Macias, T.; Misra, M.; Patel, M.; Martini, A.; Menezes, P. L.  
469 Physicochemical and tribological comparison of bio-and halogen-based ionic liquid lu-  
470 bricants. *J. Mol. Liq.* **2022**, 120918.

- 471 (24) Gabler, C.; Tomastik, C.; Brenner, J.; Pisarova, L.; Doerr, N.; Allmaier, G. Corrosion  
472 properties of ammonium based ionic liquids evaluated by SEM-EDX, XPS and ICP-  
473 OES. *Green Chem.* **2011**, *13*, 2869–2877.
- 474 (25) Ma, Y.; Han, F.; Li, Z.; Xia, C. Corrosion behavior of metallic materials in acidic-  
475 functionalized ionic liquids. *ACS Sustainable Chem. Eng.* **2016**, *4*, 633–639.
- 476 (26) Zunita, M.; Wahyuningrum, D.; Buchari; Bundjali, B.; Wenten, I. G.; Boopathy, R.  
477 Corrosion inhibition performances of imidazole derivatives-based new ionic liquids on  
478 carbon steel in brackish water. *Appl. Sci.* **2020**, *10*, 7069.
- 479 (27) Su, H.; Wang, L.; Wu, Y.; Zhang, Y.; Zhang, J. Insight into inhibition behavior of  
480 novel ionic liquids for magnesium alloy in NaCl solution: Experimental and theoretical  
481 investigation. *Corros. Sci.* **2020**, *165*, 108410.
- 482 (28) Deyab, M.; Mohsen, Q. Understanding the anticorrosion mechanism of phosphonium  
483 based ionic liquid for steel in brine water containing H<sub>2</sub>S and CO<sub>2</sub>. *J. Mol. Liq.* **2021**,  
484 *321*, 114921.
- 485 (29) Zeng, X.; Zheng, X.; Guo, L.; Xu, Q.; Huang, H.; Tan, B. Three imidazole ionic liquids  
486 as green and eco-friendly corrosion inhibitors for mild steel in sulfuric acid medium. *J.*  
487 *Mol. Liq.* **2021**, *324*, 115063.
- 488 (30) Mobin, M.; Aslam, R.; Salim, R.; Kaya, S. An investigation on the synthesis, char-  
489 acterization and anti-corrosion properties of choline based ionic liquids as novel and  
490 environmentally friendly inhibitors for mild steel corrosion in 5% HCl. *J. Colloid In-*  
491 *terface Sci.* **2022**, *620*, 293–312.
- 492 (31) Yu, Q.; Zhang, C.; Dong, R.; Shi, Y.; Wang, Y.; Bai, Y.; Zhang, J.; Cai, M.; Zhou, F.  
493 Novel N, P-containing oil-soluble ionic liquids with excellent tribological and anti-  
494 corrosion performance. *Tribol. Int.* **2019**, *132*, 118–129.



- 495 (32) Su, H.; Wu, Y.; Zhang, Y.; Jiang, Y.; Ding, Y.; Wang, L.; Zhang, J. Enhancing the long-  
496 term anti-corrosion property of Mg alloy by quaternary phosphonium salt: Integrated  
497 experimental and theoretical approaches. *Corros. Sci.* **2021**, *178*, 109010.
- 498 (33) Deyab, M.; Mohsen, Q. Impact of phosphonium-based ionic liquid on the corrosion  
499 control of aluminum alloy AA5052 in MED desalination plants during acid cleaning  
500 process. *J. Mol. Liq.* **2021**, *334*, 116121.
- 501 (34) Verma, C.; Ebenso, E. E.; Quraishi, M. Ionic liquids as green and sustainable corrosion  
502 inhibitors for metals and alloys: an overview. *J. Mol. Liq.* **2017**, *233*, 403–414.
- 503 (35) Zunita, M.; Kevin, Y. J. Ionic liquids as corrosion inhibitor: from research and devel-  
504 opment to commercialization. *Results Eng.* **2022**, 100562.
- 505 (36) Gurjar, S.; Sharma, S. K.; Sharma, A.; Ratnani, S. Performance of imidazolium based  
506 ionic liquids as corrosion inhibitors in acidic medium: A review. *Appl, Sur. Sci. Adv.*  
507 **2021**, *6*, 100170.
- 508 (37) Ardakani, E. K.; Kowsari, E.; Ehsani, A.; Ramakrishna, S. Performance of all ionic  
509 liquids as the eco-friendly and sustainable compounds in inhibiting corrosion in various  
510 media: A comprehensive review. *Microchem. J.* **2021**, *165*, 106049.
- 511 (38) Uerdingen, M.; Treber, C.; Balser, M.; Schmitt, G.; Werner, C. Corrosion behaviour of  
512 ionic liquids. *Green Chem.* **2005**, *7*, 321–325.
- 513 (39) Dilasari, B.; Jung, Y.; Sohn, J.; Kim, S.; Kwon, K. Review on corrosion behavior of  
514 metallic materials in room temperature ionic liquids. *Int. J. Electrochem. Sci.* **2016**,  
515 *11*, 1482–1495.
- 516 (40) Perissi, I.; Bardi, U.; Caporali, S.; Lavacchi, A. High temperature corrosion properties  
517 of ionic liquids. *Corros. Sci.* **2006**, *48*, 2349–2362.

- 518 (41) Wu, K.; Zhou, X.; Wu, X.; Lv, B.; Jing, G.; Zhou, Z. Understanding the corrosion  
519 behavior of carbon steel in amino-functionalized ionic liquids for CO<sub>2</sub> capture assisted  
520 by weight loss and electrochemical techniques. *Int. J. Greenhouse Gas Control* **2019**,  
521 *83*, 216–227.
- 522 (42) Pisarova, L.; Gabler, C.; Dörr, N.; Pittenauer, E.; Allmaier, G. Thermo-oxidative sta-  
523 bility and corrosion properties of ammonium based ionic liquids. *Tribol. Int.* **2012**, *46*,  
524 73–83.
- 525 (43) Wang, Y.-C.; Lee, T.-C.; Lin, J.-Y.; Chang, J.-K.; Tseng, C.-M. Corrosion properties  
526 of metals in dicyanamide-based ionic liquids. *Corros. Sci.* **2014**, *78*, 81–88.
- 527 (44) Dilasari, B.; Jung, Y.; Kwon, K. Comparative study of corrosion behavior of metals in  
528 protic and aprotic ionic liquids. *Electrochem. Commun.* **2016**, *73*, 20–23.
- 529 (45) Popoola, L. T. Progress on pharmaceutical drugs, plant extracts and ionic liquids as  
530 corrosion inhibitors. *Heliyon* **2019**, *5*, e01143.
- 531 (46) Zhang, Q.; Hua, Y. Corrosion inhibition of mild steel by alkyimidazolium ionic liquids  
532 in hydrochloric acid. *Electrochim. Acta* **2009**, *54*, 1881–1887.
- 533 (47) Qiang, Y.; Zhang, S.; Guo, L.; Zheng, X.; Xiang, B.; Chen, S. Experimental and  
534 theoretical studies of four allyl imidazolium-based ionic liquids as green inhibitors for  
535 copper corrosion in sulfuric acid. *Corros. Sci.* **2017**, *119*, 68–78.
- 536 (48) Kobzar, Y. L.; Fatyeyeva, K. Ionic liquids as green and sustainable steel corrosion  
537 inhibitors: Recent developments. *Chem. Eng. J.* **2021**, *425*, 131480.
- 538 (49) Espinosa, T.; Sanes, J.; Jiménez, A.-E.; Bermúdez, M.-D. Surface interactions, corrosion  
539 processes and lubricating performance of protic and aprotic ionic liquids with OFHC  
540 copper. *Applied Surf. Sci.* **2013**, *273*, 578–597.

- 541 (50) Westerholt, A.; Weschta, M.; Bosmann, A.; Tremmel, S.; Korth, Y.; Wolf, M.;  
542 Schlucker, E.; Wehrum, N.; Lennert, A.; Uerdingen, M.; others Halide-free synthesis  
543 and tribological performance of oil-miscible ammonium and phosphonium-based ionic  
544 liquids. *ACS Sustainable Chem. Eng.* **2015**, *3*, 797–808.
- 545 (51) Fraser, K. J.; MacFarlane, D. R. Phosphonium-based ionic liquids: an overview. *Aust.*  
546 *J. Chem.* **2009**, *62*, 309–321.
- 547 (52) Khazalpour, S.; Yarie, M.; Kianpour, E.; Amani, A.; Asadabadi, S.; Seyf, J. Y.; Reza-  
548 eivala, M.; Azizian, S.; Zolfigol, M. A. Applications of phosphonium-based ionic liquids  
549 in chemical processes. *J. Iran. Chem. Soc.* **2020**, *17*, 1775–1917.
- 550 (53) Reeves, C. J.; Siddaiah, A.; Menezes, P. L. Friction and wear behavior of environmen-  
551 tally friendly ionic liquids for sustainability of biolubricants. *J. Tribol.* **2019**, *141*.
- 552 (54) Kasar, A. K.; Rahman, M. H.; D’Souza, B.; Menezes, P. L. Tribological performance  
553 of ionic liquid impregnated porous aluminum borate ceramic. *Tribol. Int.* **2023**, *180*,  
554 108219.
- 555 (55) Silverstein, R. M.; Bassler, G. C. Spectrometric identification of organic compounds.  
556 *Journal of Chemical Education* **1962**, *39*, 546.
- 557 (56) Martínez, L.; Andrade, R.; Birgin, E. G.; Martínez, J. M. PACKMOL: A package for  
558 building initial configurations for molecular dynamics simulations. *J. Comput. Chem.*  
559 **2009**, *30*, 2157–2164.
- 560 (57) Haris, N. I. N.; Sobri, S.; Yusof, Y. A.; Kassim, N. K. An overview of molecular dynamic  
561 simulation for corrosion inhibition of ferrous metals. *Metals* **2020**, *11*, 46.
- 562 (58) Plimpton, S. Fast parallel algorithms for short-range molecular dynamics. *J. Comput.*  
563 *Phys.* **1995**, *117*, 1–19.

- 564 (59) Zhang, B.; van Duin, A. C.; Johnson, J. K. Development of a ReaxFF reactive force  
565 field for tetrabutylphosphonium glycinate/CO<sub>2</sub> mixtures. *J. Phys. Chem. B* **2014**, *118*,  
566 12008–12016.
- 567 (60) Khajeh, A.; Hu, X.; Mohammadtabar, K.; Shin, Y. K.; Van Duin, A. C.; Berkebile, S.;  
568 Martini, A. Statistical analysis of tri-cresyl phosphate conversion on an iron oxide  
569 surface using reactive molecular dynamics simulations. *J. Phys. Chem. C* **2019**, *123*,  
570 12886–12893.
- 571 (61) Khajeh, A.; Bhuiyan, F. H.; Mogonye, J.-E.; Pesce-Rodriguez, R. A.; Berkebile, S.;  
572 Martini, A. Thermal decomposition of tricresyl phosphate on ferrous surfaces. *J. Phys.*  
573 *Chem. C* **2021**, *125*, 5076–5087.
- 574 (62) Evans, D. J.; Holian, B. L. The nose–hoover thermostat. *J. Comput. Phys.* **1985**, *83*,  
575 4069–4074.
- 576 (63) Chinglenthoba, C.; Joseph, A.; Mecheri, P.; Vandana, S. Enhanced corrosion resistance  
577 of ABS: bamboo fibre electrospun membrane filtered biodiesel. *J. Bio- Tribo-Corros.*  
578 **2020**, *6*, 1–7.
- 579 (64) Floyd, F. L.; Tatti, S.; Provder, T. Using DC electrochemical techniques to assess the  
580 relative corrosiveness of water-based coatings and their ingredients. *J. Coat. Technol.*  
581 *Res.* **2007**, *4*, 111–129.
- 582 (65) Instrument, G. Electrochemical Techniques for Corrosion Measurement. [https://www.  
583 gamry.com/assets/Uploads/Echem-Corrosion-Measurement.pdf](https://www.gamry.com/assets/Uploads/Echem-Corrosion-Measurement.pdf).
- 584 (66) Tait, W. S. *Handbook of environmental degradation of materials*; Elsevier, 2018; pp  
585 97–115.
- 586 (67) Esmailzadeh, S.; Aliofkhazraei, M.; Sarlak, H. Interpretation of cyclic potentiodynamic

- 587 polarization test results for study of corrosion behavior of metals: a review. *Prot. Met.*  
588 *Phys. Chem. Surf.* **2018**, *54*, 976–989.
- 589 (68) Pankratz, R.; Bandelin, F. The colorimetric determination of salicylates. *J. Am. Pharm.*  
590 *Assoc.* **1952**, *41*, 267–270.
- 591 (69) Hernández, H. H.; Reynoso, A. R.; González, J. T.; Morán, C. G.; Hernández, J. M.;  
592 Ruiz, A. M.; Hernández, J. M.; Cruz, R. O. Electrochemical impedance spectroscopy  
593 (EIS): A review study of basic aspects of the corrosion mechanism applied to steels.  
594 *Electrochemical Impedance Spectroscopy* **2020**, 137–144.
- 595 (70) Liu, T.; Rahman, M. H.; Menezes, P. L.; Martini, A. Effect of Ion Pair on Contact  
596 Angle for Phosphonium Ionic Liquids. *J. Phys. Chem. B* **2022**, *126*, 4354–4363.
- 597 (71) Otero, R.; de Parga, A. V.; Gallego, J. M. Electronic, structural and chemical effects  
598 of charge-transfer at organic/inorganic interfaces. *Surface Science Reports* **2017**, *72*,  
599 105–145.
- 600 (72) Scheiner, S.; Hellmich, C. Stable pitting corrosion of stainless steel as diffusion-  
601 controlled dissolution process with a sharp moving electrode boundary. *Corrosion sci-*  
602 *ence* **2007**, *49*, 319–346.
- 603 (73) Gutman, M.; Nachliel, E.; Friedman, R. The mechanism of proton transfer be-  
604 tween adjacent sites on the molecular surface. *Biochimica et Biophysica Acta (BBA)-*  
605 *Bioenergetics* **2006**, *1757*, 931–941.
- 606 (74) Kumar, P.; No-Lee, H.; Kumar, R. Synthesis of phase pure iron oxide polymorphs thin  
607 films and their enhanced magnetic properties. *Journal of Materials Science: Materials*  
608 *in Electronics* **2014**, *25*, 4553–4561.
- 609 (75) Nguyen, E.; Chrimes, A.; Brkljača, R.; Ou, J.; Berean, K.; Zhuiykov, S.; Kalan-  
610 tarzadeh, K. Assessment of a Raman micro-spectroscopy/microfluidics unit using

- 611 a model E. coli/glucose bio-system. The 7th IEEE International Conference on  
612 Nano/Molecular Medicine and Engineering. 2013; pp 157–162.
- 613 (76) Risi, R.; Manti, L.; Perna, G.; Lasalvia, M.; Capozzi, V.; Delfino, I.; Lepore, M. X-ray  
614 radiation-induced effects in human mammary epithelial cells investigated by Raman  
615 microspectroscopy. *Biophotonics: Photonic solutions for better Health care III*. 2012;  
616 pp 437–446.
- 617 (77) Konovalova, V. The effect of temperature on the corrosion rate of iron-carbon alloys.  
618 *Materials Today: Proceedings* **2021**, *38*, 1326–1329.
- 619 (78) Guo, Q.; Cocks, I.; Williams, E. The adsorption of benzoic acid on a TiO<sub>2</sub> (110) surface  
620 studied using STM, ESDIAD and LEED. *Surf. Sci.* **1997**, *393*, 1–11.
- 621 (79) del Arco, M.; Gutiérrez, S.; Martín, C.; Rives, V.; Rocha, J. Synthesis and charac-  
622 terization of layered double hydroxides (LDH) intercalated with non-steroidal anti-  
623 inflammatory drugs (NSAID). *J. Solid State Chem.* **2004**, *177*, 3954–3962.
- 624 (80) Morosanova, M. A.; Morosanova, E. I. Silica-titania xerogel for solid phase spectropho-  
625 tometric determination of salicylate and its derivatives in biological liquids and phar-  
626 maceuticals. *Chem. Cent. J.* **2015**, *9*, 1–8.
- 627 (81) Ata, M.; Liu, Y.; Zhitomirsky, I. A review of new methods of surface chemical modi-  
628 fication, dispersion and electrophoretic deposition of metal oxide particles. *RSC Adv.*  
629 **2014**, *4*, 22716–22732.
- 630 (82) Roy, S.; Kästner, J. Synergistic substrate and oxygen activation in salicylate dioxyge-  
631 nase revealed by QM/MM simulations. *Angew. Chem., Int. Ed.* **2016**, *55*, 1168–1172.
- 632 (83) Van der Horn, J. A.; Souvignier, B.; Lutz, M. Crystallization, Structure Determination  
633 and Reticular Twinning in Iron (III) Salicylate: Fe[(HSal)(Sal)(H<sub>2</sub>O)<sub>2</sub>]. *Crystals* **2017**,  
634 *7*, 377.

- 635 (84) Bucci, R.; Carunchio, V.; Girelli, A. Formation of iron (II) complexes with some aro-  
636 matic anions in DMSO. *Inorg. Chim. Acta* **1988**, *141*, 99–102.
- 637 (85) Mendonça, A. C.; Malfreyt, P.; Padua, A. A. Interactions and ordering of ionic liquids  
638 at a metal surface. *J. Chem. Theory Comput.* **2012**, *8*, 3348–3355.
- 639 (86) Sobota, M.; Nikiforidis, I.; Hieringer, W.; Paape, N.; Happel, M.; Steinruck, H.-P.;  
640 Gorling, A.; Wasserscheid, P.; Laurin, M.; Libuda, J. Toward ionic-liquid-based model  
641 catalysis: growth, orientation, conformation, and interaction mechanism of the [Tf<sub>2</sub>N]-  
642 anion in [BMIM][Tf<sub>2</sub>N] thin films on a well-ordered alumina surface. *Langmuir* **2010**,  
643 *26*, 7199–7207.
- 644 (87) Xu, S.; Xing, S.; Pei, S.-S.; Baldelli, S. Sum frequency generation spectroscopy study  
645 of an ionic liquid at a graphene-BaF<sub>2</sub> (111) interface. *J. Phys. Chem. B* **2014**, *118*,  
646 5203–5210.
- 647 (88) Senftle, T. P.; Hong, S.; Islam, M. M.; Kylasa, S. B.; Zheng, Y.; Shin, Y. K.; Junker-  
648 meier, C.; Engel-Herbert, R.; Janik, M. J.; Aktulga, H. M.; others The ReaxFF reactive  
649 force-field: development, applications and future directions. *npj Comput. Mater.s* **2016**,  
650 *2*, 1–14.

651 TOC Graphic

652

